NOD1 is a key mediator of atrial myopathy in heart failure

Marta Gil-Fernández,[1] Almudena Val-Blasco,[1,†] Andrea Bueno-Sen,[1,†] Paula Cantolla-Pablo,[1,†] Carlos Galán-Arriola,[2,12] Ali Ayaon,[3] Teresa López-Fernández,[1,3] Yuriana Aguilar-Sanchez,[4] Satadru K Lahiri,[4] José Alberto Navarro-García,[4] Rafael Peinado,[1,3] Angel Aroca,[3] Miguel Ángel Rubio,[3] José Antonio Blázquez,[5] María Tamayo,[6] Eduardo López-Collazo,[1] Gema Ruiz-Hurtado,[7,10,12] Inmaculada Jorge,[2,12] Jesús Vázquez,[2,12] Patricia Prieto,[8,12] Tarik Smani,[9] Antonio Ordoñez,[9] David Filgueiras-Dama,[2,12] Raúl Moreno,[1,3] Borja Rivero-Santana,[1,3] Jorge Nuche,[2,12,16] José Jalife,[2,12,15] Borja Ibáñez,[2,11,12] Carmen Delgado,[6,12] Lisardo Boscá,[6,12*] Xander H.T. Wehrens,[4,13,14*] María Fernández-Velasco,[1,12*]

[1]Hospital La Paz Institute for Health Research (IdiPAZ), Madrid, Spain; [2]Spanish National Centre for Cardiovascular Research (CNIC), Madrid, Spain; [3]La Paz University Hospital, Madrid, Spain; [4]Cardiovascular Research Institute, Baylor College of Medicine, Houston, TX, USA; [5]Salamanca University Hospital (CAUSA), Salamanca, Spain; [6]Sols-Morreale Biomedical Research Institute (IIBM, CSIC-UAM), Madrid, Spain; [7]Cardiorenal Translational Laboratory, Research Institute Hospital 12 de Octubre (i+12), Madrid, Spain; [8]Pharmacology Department, Pharmacy Faculty, Complutense University of Madrid (UAM), Spain; [9]Cardiovascular Pathophysiology group, Institute of Biomedicine of Seville (IBiS), Virgen del Rocío University Hospital /University of Seville/CSIC, Seville, Spain; [10]Department of Physiology, Autonomous University of Madrid, Spain; [11]Cardiology Department, Fundación Jiménez Diaz University Hospital Health Research Institute (IIS-FJD), Madrid, Spain; [12]Cardiovascular Biomedical Research Centre Network (CIBERCV), Madrid, Spain; [13]Department of Integrative Physiology, Baylor College of Medicine, Houston, TX, USA; [14]Department of Medicine, Baylor College of Medicine, Houston, TX, USA; [15]Departments of Medicine and Molecular & Integrative Physiology, University of Michigan, Ann Arbor (J.J.),

USA; [16]Cardiology Department, 12 de Octubre University Hospital, Research Institute Hospital 12 de Octubre (i+12). Madrid, Spain.

*Address for correspondence:

María Fernández Velasco, Hospital La Paz Institute for Health Research (IdiPAZ), Paseo de la Castellana, 261 28046 Madrid, Spain; Tel: +34 91 727 75 30

Email: maria.fernandez@idipaz.es; mfvlorenzo@gmail.com

Xander H.T. Wehrens, Baylor College of Medicine, 1 Baylor Plaza 77030, Houston, Texas, USA; Tel: 713-798-4182

Email: wehrens@bcm.edu

Lisardo Boscá, Sols-Morreale Biomedical Research Institute (IIBM), Arturo Duperier, 4, Fuencarral-El Pardo, 28029 Madrid, Spain; Tel: +34 91 497 2747

Email: lbosca@iib.uam.es

Authorship notes

† These authors contributed equally to the study.

Keywords

NOD1, atrial remodeling, heart failure, innate immunity, CaMKII, RyR2

Abstract

Heart failure (HF)-associated atrial myopathy is driven by complex and poorly understood mechanisms. Emerging evidence suggests that innate immune components contribute to atrial remodeling, yet the role of nucleotide-binding oligomerization domain-containing protein 1 (NOD1) receptors remains unclear.

Methods: NOD1 expression was characterized in atrial myocardium of HF patients (n = 36) and non-failing controls (n = 45) undergoing valve surgery, and in two porcine models of atrial myopathy with divergent ventricular phenotypes: aortic banding (AoB; preserved LVEF) and left atrial infarction (LAI; reduced LVEF). The causal role of NOD1 in atrial remodeling was assessed using genetic (*Nod1*$^{-/-}$) and pharmacological (ML-130) loss-of-function approaches in a murine transverse aortic constriction (TAC) model, and through selective NOD1 activation with C12-iE-DAP in wild-type, *Nod1*$^{-/-}$, and *RyR2*-S2814A mice. Proteomic, phosphoproteomic, transcriptomic, and Ca^{2+} imaging analyses were performed across experimental systems.

Results: NOD1 was markedly upregulated in atrial myocardium of HF patients and in both porcine models, across divergent ventricular phenotypes and irrespective of documented rhythm status, correlating with structural and functional indices of atrial disease severity. Genetic NOD1 deficiency in TAC mice prevented atrial dysfunction, structural remodeling, activation of profibrotic molecular pathways and Ca^{2+} mishandling. Pharmacological NOD1 inhibition with ML-130 reproduced the protective effects on atrial structural and Ca^{2+} handling. Selective NOD1 activation with C12-iE-DAP induced atrial Ca^{2+} dysregulation through CaMKII-dependent RyR2-Ser2814 hyperphosphorylation, effects that were abrogated by CaMKII inhibition, and absent in *RyR2*-S2814A mice. Human atrial transcriptomic analysis confirmed enrichment of inflammatory, Ca^{2+}-signaling, and extracellular matrix remodeling

pathways in HF. Increased CaMKII phosphorylation in human atrial myocardium further corroborated the translational relevance of the NOD1–CaMKII–RyR2 axis.

Conclusions: These findings identify the NOD1–CaMKII–RyR2 axis as a cardiomyocyte-centered mechanism linking innate immune activation to atrial Ca^{2+} dysregulation and structural remodeling in HF, establishing NOD1 as a molecular indicator of atrial myopathy burden and a mechanism-based therapeutic target.

Graphical abstract

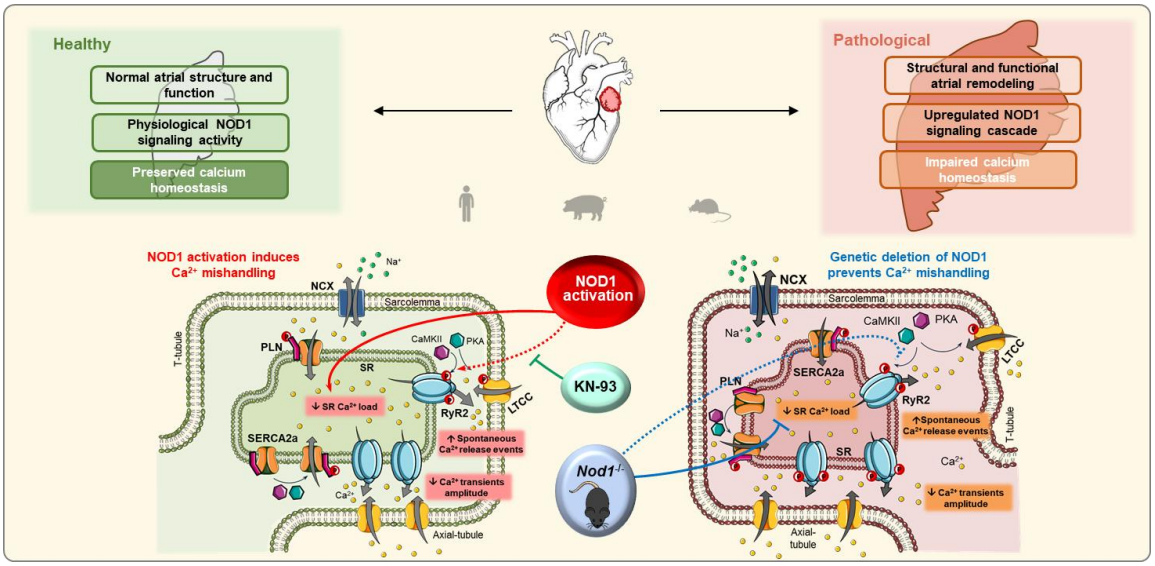

Introduction

Heart failure (HF) is a complex syndrome and a leading cause of global morbidity and mortality. Chronic elevation of left ventricular (LV) filling pressures promotes maladaptive remodeling of the left atrium (LA), characterized by chamber enlargement and functional impairment [1]. While ventricular remodeling has been extensively studied [2,3], the molecular mechanisms driving atrial myopathy remain incompletely defined.

Atrial myopathy encompasses structural and functional alterations with substantial clinical implications [4]. It may occur independently of atrial fibrillation (AF) [4], although atrial remodeling creates an arrhythmogenic substrate that facilitates AF initiation and maintenance [5,6]. Approximately half of patients with chronic HF exhibit moderate to severe LA enlargement, a powerful predictor of all-cause mortality, cardiovascular death, and hospitalization [7]. Advances in cardiac imaging, particularly speckle-tracking echocardiography, have enabled detailed evaluation of atrial reservoir, conduit, and contractile function [8,9]. Strain-based indices derived from these assessments have emerged as robust prognostic markers in HF, identifying subclinical atrial dysfunction that precedes overt remodeling [10]. These observations highlight the clinical relevance of identifying the molecular mechanisms underlying atrial dysfunction to refine risk stratification and enable targeted therapy in HF.

Inflammation and innate immune activation are increasingly recognized as key contributors to HF-associated atrial myopathy [11,12]. Pattern recognition receptors (PRRs) detect pathogen-associated and damage-associated molecular patterns (PAMPs and DAMPs), activating inflammatory cascades that can compromise cardiac homeostasis [13,14]. Among PRRs, nucleotide-binding oligomerization domain (NOD)-like receptors (NLRs) have emerged as critical regulators of myocardial inflammation, arrhythmogenesis, and HF

progression [15–19]. Persistent innate immune activation in HF drives atrial inflammation and disrupts intracellular Ca^{2+} handling, contributing to atrial dysfunction and remodeling [15]. While the NLRP3 inflammasome is a well-established contributor to atrial remodeling and AF [13,14], the role of nucleotide-binding oligomerization domain-containing protein 1 (NOD1) in HF-associated atrial myopathy remains unclear. NOD1 is a cytosolic PRR that, upon activation, recruits receptor-interacting serine/threonine-protein kinase 2 (RIP2), triggering an NF-κB-dependent inflammatory response [18].

This study identifies NOD1 as a mechanistic contributor to atrial myopathy by integrating human atrial tissue analysis with large-animal and murine HF models. Mechanistically, NOD1 activation enhances CaMKII-dependent phosphorylation of RyR2, promoting sarcoplasmic reticulum Ca^{2+} leak and driving progressive atrial damage. These findings point to NOD1 as a new mechanistic pathway involved in atrial remodeling and a potential therapeutic target in HF-associated atrial myopathy, highlighting its role in connecting innate immune signaling with Ca^{2+} dysregulation and structural remodeling.

Materials and Methods

Study approval

The human study protocol was approved by the Human Ethics Committee of La Paz University Hospital (CEIm: 1729) and conducted in accordance with the principles of the Declaration of Helsinki. All participants provided written informed consent prior to inclusion. All animal experiments were approved by the General Direction of Agriculture and Environment and conducted in accordance with Spanish regulations and EU Directive 2010/63/EU (PROEX 103/19 for pigs and PROEX 053/18 for mice).

Human studies

The cohort included 81 patients undergoing valve surgery: 45 non-failing patients (NF; NT-proBNP < 200 pg/mL, LVEF > 50%) and 36 with HF (including HFmrEF and HFrEF; NT-proBNP ≥ 200 pg/mL, LVEF ≤ 50%). Detailed clinical and echocardiographic parameters are presented in Table 1.

Left or right atrial (LA and RA) appendages were collected intraoperatively, snap-frozen, and stored at −80 °C or processed for molecular, transcriptomic, and histological analyses. Echocardiographic studies were performed according to the American Society of Echocardiography (ASE) and European Association of Cardiovascular Imaging (EACVI) guidelines. Further details on clinical, imaging, and RNA sequencing procedures are provided in the Supplementary Methods.

Animal studies

Swine models

Two independent models were used to induce atrial remodeling secondary to mechanical overload or ischemic injury: (1) aortic banding (AoB) was performed in male Yucatan minipigs (n = 13), inducing progressive pressure overload with preserved LVEF; and (2) left atrial infarction (LAI) in male Large White pigs (n = 21), resulting in atrial dysfunction with reduced LVEF.

A subset of LAI animals (n = 6) underwent dual-chamber pacemaker implantation and atrioventricular (AV) node ablation to enable controlled AF induction by burst pacing. Sham-operated animals served as controls for AoB (n = 17) and LAI (n = 14). Animals were monitored for 32 weeks (AoB model) or 8 weeks (LAI model) post-surgery, after which LA tissue was collected for analysis.

Cardiac magnetic resonance (CMR) imaging was performed to evaluate cardiac function, including reservoir, conduit, and contractile function. Detailed surgical and imaging protocols are described in the Supplementary Methods.

Mouse studies

Transverse aortic constriction (TAC) was performed in male wild-type (WT) and *Nod1*$^{-/-}$ mice on a C57BL/6J background to induce pressure overload. Sham-operated mice underwent identical procedures without constriction. Successful *Nod1* knockout was confirmed by genotyping (Figure S1). Atrial tissue was collected 4 weeks after TAC.

A subset of WT-Sham and WT-TAC mice was treated with the selective NOD1 inhibitor ML-130 (ML; 2 mg/kg, i.p.) every other day for 4 weeks. Pharmacological studies further comprised daily intraperitoneal administration of saline or the NOD1 agonist C12-iE-DAP (iE; 3.3 mg/kg, i.p.) in WT, *Nod1*$^{-/-}$, and *RyR2*-S2814A mice for 3 days. The CaMKII inhibitor KN-93 93 (KN; 2.7 mg/kg, i.p.), alone or in combination with C12-iE-DAP, was administered exclusively to WT mice for 3 days.

Echocardiography and CMR were performed to assess cardiac function. Additionally, atrial cardiomyocytes were isolated and examined by confocal microscopy to measure Ca^{2+} transients, SR Ca^{2+} load, and spontaneous sparks. Proteomic and phosphoproteomic analyses were performed using TMT18-plex labeling and Orbitrap Fusion LC-MS/MS. Further methodological details are available in the Supplementary Methods.

Artificial intelligence (AI) tool usage declaration

The authors declare that Microsoft Copilot was used solely for language editing and improvement of English grammar of the manuscript.

Statistical analysis

Data are presented as mean ± SEM. Normality was verified by Kolmogorov-Smirnov and Shapiro-Wilk tests. Between-group comparisons were performed using unpaired Student's *t*-tests, χ^2 tests, one-way or two-way ANOVA followed by Tukey's post hoc test, or nested ANOVA as appropriate. A $P < 0.05$ was considered statistically significant. Correlations were assessed using Pearson's correlation coefficient for normally distributed data. Analyses were performed using GraphPad Prism 9 (GraphPad Software Inc., San Diego, CA, USA), Origin Pro v9.0 (OriginLab Corp., Northampton MA, USA), or SPSS22 (IBM, Armonk, NY, USA).

Results

NOD1 signaling is upregulated in atrial myocardium of HF patients

The study cohort comprised 81 patients undergoing valve surgery, stratified into NF (n = 45) and HF (n = 36) groups based on LVEF and NT-proBNP levels. Consistent with these criteria, HF patients showed significantly lower LVEF and elevated NT-proBNP levels compared with NF controls (Figure S2A). Baseline demographics and comorbidities were comparable between groups; however, HF patients more frequently presented with higher NYHA class III/IV and greater diuretic use (Table 1).

Echocardiographic assessment revealed marked atrial and ventricular remodeling in HF patients, characterized by increased LV volumes, elevated pulmonary pressures, and a higher E/E′ ratio (Table 1). Two-dimensional speckle-tracking demonstrated biatrial enlargement, with increased maximal and minimal LA and RA volumes accompanied by impaired reservoir, conduit, and contractile strain (Figure S2B-C). These structural and functional atrial abnormalities were associated with higher operative risk, as reflected by EuroSCORE (Figure S2D). Masson's Trichrome staining of atrial samples suggested increased collagen deposition in HF patients compared with NF controls (Figure S3A).

Immunohistochemistry revealed NOD1 localization within atrial cardiomyocytes (Figure 1A), with no evidence of macrophage, T cell, or B cell infiltration in atrial myocardial biopsies from either HF or NF patients (Figure S2E). Western blot analysis showed increased protein levels of NOD1 and its adaptor RIP2, together with elevated levels of inflammatory cytokines IL-1β and IL-6 in HF atrial tissue (Figure 1B). Although the incidence of documented AF was higher in HF patients (Figure 1C), subgroup analysis of HF stratified by rhythm status at the time of preoperative evaluation demonstrated comparable NOD1 protein levels between those in sinus rhythm and those with AF (Figure 1D), suggesting that NOD1 upregulation in the failing atrium is not contingent upon documented AF.

Next, atrial NOD1 protein levels were matched to chamber-specific echocardiographic features. NOD1 expression positively correlated with maximal and minimal atrial volumes, and inversely with atrial reservoir strain (Figure 1E). Additional correlations with atrial area, conduit and contractile strain, NT-proBNP levels, and EuroSCORE further highlighted the clinical relevance of NOD1 upregulation in failing human atria (Figure S2F-G).

Collectively, these findings establish NOD1 upregulation as a molecular hallmark of atrial remodeling in human HF, bridging innate immune activation with structural and functional atrial damage.

NOD1 expression is increased in swine models of atrial myopathy

NOD1 expression was next assessed in two swine models of atrial myopathy: aortic banding (AoB), with preserved LVEF, and left atrial infarction (LAI), with reduced LVEF (Figure S4A). Despite the differences in ventricular phenotypes, CMR imaging confirmed significant atrial impairment in both models, including increased LA volumes and areas, reduced LA strain, and mild RA dysfunction (Figure S4B-G and Tables 2 and 3).

Immunohistochemical analysis of LA tissue from AoB and LAI swine revealed prominent NOD1 staining in atrial cardiomyocytes (Figure 1F), with no detectable macrophage, T cell, or B cell infiltration (Figure S4H-I). Western blot analyses confirmed elevated levels of NOD1 and RIP2 in LA tissue from both LAI and AoB models compared to their respective controls (Figure 1G-I). These molecular changes were accompanied by increased expression of *IL1B* and *IL6* in failing atria from both models (Figure S5A-B). Notably, in an independent LAI cohort designed for electrophysiological studies, NOD1 protein levels were comparable between animals subjected to sustained burst pacing-induced AF and those maintained under sinus rhythm conditions (Figure 1J).

Consistent with the human data, significant correlations were observed in both swine models between LA NOD1 protein levels and maximal and minimal atrial volumes, as well as atrial reservoir strain (Figure 1K). Additional associations with conduit and contractile strain further reinforced the pathophysiological relevance of NOD1 in atrial remodeling (Figure S5C-D).

Together, these results demonstrate that atrial NOD1 upregulation is a conserved feature of HF-associated atrial remodeling, observed across divergent ventricular phenotypes and irrespective of documented rhythm status.

<u>NOD1 deficiency prevents atrial remodeling and Ca^{2+}mishandling in pressure-overload mice</u>

To elucidate the role of NOD1 in atrial remodeling, we employed a genetic loss-of-function approach using a murine pressure-overload model of HF induced by TAC (Figure S6A). NOD1 deficiency prevented pressure overload–induced atrial remodeling. Additionally, *Nod1*$^{-/-}$ mice were protected from TAC-induced LV dysfunction (Table 4; Figure S6B).

NOD1 deficiency conferred protection against biatrial remodeling, preventing TAC-induced increases in LA and RA weights, alterations in maximal and minimal atrial volumes,

and impairment of atrial reservoir function documented in WT TAC mice (Table 4, Figure 2A-C, Figure S6C). Morphometric analyses further demonstrated that NOD1 deficiency significantly prevented TAC-induced cardiomyocyte hypertrophy (Figure 2D).

Immunohistochemistry confirmed robust NOD1 expression in LA cardiomyocytes (Figure 2E) with no macrophage, T cell, or B cell infiltration across groups (Figure S6D). qPCR analyses revealed upregulation of *Nod1* and *Rip2* transcripts, together with increased expression of *Il1b* and *Il6* in WT-TAC atria; these inflammatory markers were markedly attenuated in *Nod1*$^{-/-}$-TAC atria (Figure 2F-G).

Proteomic profiling identified 6,898 proteins, with 743 differentially expressed (FDR < 0.05) in LA tissue from WT-TAC vs. WT-Sham and 370 in WT-TAC vs. *Nod1*$^{-/-}$-TAC (Figure S6E). Heatmap clustering (Figure S6F) demonstrated different molecular signatures across groups, while enrichment analysis revealed upregulation of inflammatory, Ca^{2+}-handling, and extracellular matrix-related proteins, and downregulation of mitochondrial metabolism proteins in WT-TAC atria; these changes were prevented by NOD1 deficiency (Figure 2H and Figure S6G).

Regarding fibrosis development, Masson's Trichrome staining suggested no changes in the collagen deposition between groups (Figure S3B); however, within the extracellular matrix proteomic signature, structural collagens Col14a1 and Col18a1, and the profibrotic matricellular proteins fibronectin (Fn1) and periostin (Postn) were all significantly elevated in WT-TAC atria and attenuated in *Nod1*$^{-/-}$-TAC mice (Figure S3C). RT-PCR further confirmed transcriptional upregulation of *Tgfb1* in WT-TAC atria, which was substantially reduced in *Nod1*$^{-/-}$-TAC mice (Figure S3D). These molecular alterations support the presence of active extracellular matrix remodeling, indicating early activation of profibrotic signaling, preceding overt structural fibrosis. Within the Ca^{2+}-handling proteome, STRING network analysis

highlighted marked differences in Ca^{2+}-handling proteins between WT-TAC and *Nod1*$^{-/-}$-TAC groups (Figure 2I), and quantitative proteomics confirmed that NOD1 deficiency prevented the downregulation of RyR2 and SERCA2a observed in WT-TAC atria (Figure 3A and Figure S6H).

Phosphoproteomic analysis was performed to identify post-translational regulatory changes. This analysis detected 1,451 phosphosites, with WT-TAC atria exhibiting global hyperphosphorylation that was normalized in *Nod1*$^{-/-}$-TAC mice (Figure S6I). Notably, RyR2 emerged as a major phosphorylation hub, with phosphorylation at Ser2814 (principal CaMKII target site) markedly increased in WT-TAC but prevented in Nod1$^{-/-}$-TAC atria (Tables S1, S2 and Figure 3B). Western blot analyses validated these findings, confirming that NOD1 deficiency prevented CaMKII-RyR2 Ser2814 hyperphosphorylation (Figure 3C). In parallel, levels of the PP1 regulatory subunit PP1R3A, which modulates RyR2 dephosphorylation, were reduced in WT-TAC but preserved in *Nod1*$^{-/-}$-TAC atria (Figure S6J).

Consistent with these molecular findings, NOD1 deficiency significantly prevented TAC-induced abnormalities in atrial Ca^{2+} handling, including increased spark-mediated diastolic Ca^{2+} leak (Figure 3D), enlarged and prolonged Ca^{2+} sparks (Figure S7A), reduced SR Ca^{2+} load (Figure 3E), and decreased Ca^{2+}transient amplitude (Figure 3F), while preserving SERCA2a expression (Figure S7B).

These findings identify NOD1 as a key driver of structural, molecular, and functional atrial remodeling under pressure overload in a mouse model.

<u>Pharmacological NOD1 inhibition reproduces the protective effects of genetic NOD1 deficiency in TAC-induced atrial myopathy</u>

To determine whether pharmacological NOD1 inhibition could recapitulate the protective phenotype observed in *Nod1*$^{-/-}$-TAC mice, we treated WT-Sham and WT-TAC mice with the

selective NOD1 inhibitor ML-130 (ML; 2 mg/kg, i.p., every other day for 4 weeks). At the structural level, pharmacological NOD1 inhibition prevented the development of cardiac and atrial hypertrophy in response to pressure overload. WT-TAC mice treated with ML did not exhibit the increases in heart or atrial weight observed in untreated WT-TAC animals, and hypertrophy indices remained comparable to WT-Sham controls (Table S3). At the microscopic level, the increase in cardiomyocyte cellular area observed in WT-TAC mice was also prevented by ML treatment (Table S3). These findings closely mirror the phenotype observed in *Nod1*$^{-/-}$-TAC mice, indicating that pharmacological inhibition of NOD1 is sufficient to prevent pressure overload–induced structural atrial remodeling.

To determine whether this structural protection was accompanied by preservation of cardiomyocyte Ca^{2+} handling, atrial cardiomyocytes were isolated for functional Ca^{2+} recordings. ML treatment had no measurable effect in WT-Sham mice, which maintained physiological Ca^{2+} handling parameters (Figures 3D-F; Figure S7A), indicating that basal NOD1 activity is low in healthy atria and that its inhibition does not disrupt physiological Ca^{2+} dynamics. In contrast, ML treatment in WT-TAC mice prevented the full spectrum of TAC-induced Ca^{2+} abnormalities, reproducing the protective effects observed in *Nod1*$^{-/-}$-TAC mice. Specifically, pharmacological NOD1 inhibition normalized spark-mediated diastolic Ca^{2+} leak, Ca^{2+} transient amplitude, SR Ca^{2+} load, and Ca^{2+} spark properties (frequency and duration), while amplitude remained unchanged (Figures 3D-F; Figure S7A).

Together, these findings demonstrate that pharmacological NOD1 inhibition reproduces both the structural and Ca^{2+} handling protection observed in genetic NOD1 deficiency, supporting a main role for NOD1 signaling in TAC-induced atrial myopathy.

<u>Selective NOD1 activation induces atrial Ca^{2+} dysregulation through CaMKII-dependent RyR2-Ser2814 phosphorylation</u>

To gain a deeper understanding of the mechanistic role of NOD1 in the development of atrial remodeling, we next examined whether selective NOD1 activation is sufficient to induce atrial dysfunction and Ca^{2+} dysregulation. WT mice were treated with the selective NOD1 agonist C12-iE-DAP (iE; 3.3 mg/kg, i.p., for 3 days). Echocardiography revealed reduced LVEF and increased LA enlargement in WT mice treated with iE compared to vehicle-treated controls (Figure 4A and Figure S8A).

At the cellular level, iE administration markedly impaired systolic Ca^{2+} release, as evidenced by reduced Ca^{2+} transient amplitude (Figure 4B and E, left panel), together with decreased SR Ca^{2+} load (Figure 4C and E, central panel) in isolated LA cardiomyocytes. In parallel, iE increased diastolic Ca^{2+} leak through elevated Ca^{2+} sparks (Figure 4D and E, right panel). These alterations were absent in *Nod1*$^{-/-}$ mice treated with iE (Figure 4B-E), confirming the specificity of iE for NOD1-dependent mediation of atrial Ca^{2+} dysregulation. To identify the downstream effector mechanism, we examined RyR2 phosphorylation status. iE-treated WT mice exhibited a selective increase in CaMKII-dependent RyR2 phosphorylation at Ser2814 (Figure S8B).

To determine whether CaMKII signaling mediates the atrial Ca^{2+} mishandling induced by NOD1 activation, WT mice were co-treated with iE and the CaMKII inhibitor KN-93 (KN; 2.7 mg/kg, i.p., for 3 days). KN treatment completely prevented iE-induced Ca^{2+} handling impairment, normalizing Ca^{2+} transient amplitude, SR Ca^{2+} load, and Ca^{2+} spark-mediated diastolic Ca^{2+} leak (Figure 4B-E).

Genetic validation of RyR2-Ser2814 phosphorylation as the critical mechanistic target was obtained using *RyR2*-S2814A mice, in which serine 2814 is mutated to alanine preventing phosphorylation at this site. In this model, iE failed to induce atrial Ca^{2+} handling abnormalities (Figure 4B-E), corroborating the effects observed under pharmacological CaMKII inhibition.

Accordingly, atrial cardiomyocytes from *RyR2*-S2814A mice treated with iE exhibited Ca^{2+} transient amplitude, SR Ca^{2+} load, and Ca^{2+} spark-mediated diastolic Ca^{2+} leak comparable to those observed in vehicle-treated *RyR2*-S2814A controls. Together, these data identify CaMKII-dependent RyR2-Ser2814 phosphorylation as a central mechanistic node linking NOD1 activation to atrial Ca^{2+} dysregulation.

To determine whether acute NOD1 activation was sufficient to increase AF susceptibility, transesophageal burst pacing was performed in WT mice treated with iE or vehicle. AF was induced in 2 of 7 iE-treated animals compared with 1 of 7 vehicle-treated controls, with no significant differences in AF inducibility between groups (Figure S8C). These findings indicate that, while acute NOD1 activation is sufficient to reproduce cardiomyocyte Ca^{2+} dysregulation associated with triggered activity, the short-term pharmacological protocol does not lead to a detectable increase in AF inducibility under these experimental conditions.

Atrial myocardium from patients with HF displays CaMKII hyperactivation

To evaluate the translational relevance of these experimental findings, we performed transcriptomic profiling of atrial myocardium from HF and NF patients. RNA sequencing identified 15,508 expressed genes, with 463 genes upregulated and 184 downregulated in HF atrial tissue (FDR < 0.05). Clustering of the top 70 differentially expressed genes clearly distinguished HF from NF samples (Figure S9A and Table S4).

Consistent with the molecular signatures identified in our murine models, gene set enrichment analysis revealed significant enrichment of pathways associated with inflammation and muscle contraction/Ca^{2+} signaling in atrial myocardium from HF patients compared with NF samples (Figure 4F). Pathways related to extracellular matrix organization and cell–matrix interactions were also enriched (Figure S9B), consistent with structural remodeling in the

human atrium, whereas no significant enrichment was observed for mitochondrial metabolism or energy-related pathways (Figure S9B).

At the protein level, Western blot analysis demonstrated increased CaMKII phosphorylation (Thr-286/7) in HF atrial myocardium relative to NF controls (Figure 4G). These results establish CaMKII hyperactivation as a conserved molecular feature of human HF-associated atrial myopathy.

Discussion

HF imposes a significant clinical burden and is associated with high mortality, underscoring the need to better define the molecular mechanisms that drive disease progression. Growing evidence implicates sustained activation of innate immune receptors as a key contributor to maladaptive inflammatory signaling underlying HF-associated atrial myopathy [20]. Among NLRs, the NLRP3 inflammasome has been extensively studied for its role in cardiac inflammation and remodeling [14,16,20–22]. In contrast, the involvement of NOD1, another NLR family member, in clinical and experimental atrial myopathy remains underexplored.

Our study demonstrates marked NOD1 upregulation in atrial myocardium from HF patients and two porcine models with divergent ventricular phenotypes (AoB with preserved LVEF and LAI with reduced LVEF), with a consistent expression pattern observed across the study cohorts irrespective of documented rhythm status, suggesting that NOD1 upregulation reflects the structural and hemodynamic burden of HF-associated atrial remodeling rather than the underlying rhythm phenotype.

Immunohistochemical analysis revealed no macrophage, T cell, or B cell infiltration in atrial tissue across all species examined, positioning cardiomyocytes as the primary NOD1-expressing cellular compartment. This pattern was conserved across humans, porcine, and

murine models, supporting a primary role for cardiomyocytes in NOD1-mediated atrial remodeling, rather than secondary immune cell recruitment.

Elevated NOD1 expression in atrial myocardium from HF patients and porcine models strongly correlated with structural and functional markers of atrial remodeling, including atrial enlargement and impaired atrial strain. Atrial strain has emerged as a sensitive and promising marker of atrial dysfunction, improving diagnostic precision and independently predicting mortality in HF, irrespective of underlying etiology [23,24]. The association between NOD1 expression and both structural and functional atrial impairment highlights its potential as a clinically relevant molecular determinant of atrial pathology in HF.

AF represents the most common arrhythmia in HF and significantly increases morbidity and mortality worldwide [25]. Although AF incidence was higher among HF patients in our cohort, atrial NOD1 protein levels were comparable between HF patients with and without documented AF at the time of preoperative evaluation. This observation was mirrored in the porcine LAI model, where NOD1 expression remained similarly elevated in both LAI-AF and LAI-sr animals, suggesting that NOD1 upregulation is associated with the underlying structural atrial remodeling rather than arrhythmia *per se*. These findings are consistent with prior evidence demonstrating that atrial structural and molecular remodeling can precede AF onset and progress independently of arrhythmia burden in patients with HF [4].

The combined use of genetic loss-of-function and pharmacological inhibition approaches provides strong evidence supporting a role for NOD1 signaling in HF-associated atrial myopathy. *Nod1*$^{-/-}$ mice subjected to TAC exhibited markedly attenuated atrial enlargement and preserved atrial function compared with WT-TAC controls, supporting a role for NOD1 signaling as a key contributor to atrial remodeling under pressure overload. Notably, the absence of immune cell infiltration ($CD68^+$ macrophages, $CD3^+$ T cells, and $CD19^+$ B cells)

in atria from WT-TAC and *Nod1*$^{-/-}$-TAC mice supports a cardiomyocyte-intrinsic mechanism, consistent with the established role of PRRs as cell-autonomous inflammatory sensors within the myocardium [21]. In parallel, *Nod1*$^{-/-}$-TAC mice displayed attenuated LV dysfunction, suggesting that part of the observed atrial protection may be secondary to improved ventricular performance. Importantly, complementary gain-of-function experiments *in vivo* using the selective NOD1 agonist C12-iE-DAP induced atrial Ca^{2+} dysregulation in otherwise healthy mice, in the absence of overt HF or LV impairment, as previously reported [17]. Together, these findings support a cardiomyocyte-centered role for NOD1 in atrial Ca^{2+} handling, independent of hemodynamic confounders.

In parallel, structural remodeling was also evident at the level of the extracellular matrix. In human atrial samples, transcriptomic profiling revealed enrichment of pathways related to extracellular matrix organization and cell–matrix interactions. In the murine model, the analyses demonstrated that NOD1 deficiency in TAC mice prevented the dysregulation of extracellular matrix component expression, including fibrillar collagens, fibronectin, and periostin compared with the WT-TAC group. These findings indicate that NOD1 might contribute to structural remodeling in atrial myopathy.

While cardiomyocytes represent a major site of NOD1 expression in the atrium, NOD1 is also expressed in cardiac fibroblasts and endothelial cells, suggesting that NOD1 signaling in non-cardiomyocyte populations may further modulate atrial remodeling. The present study, however, primarily supports a cardiomyocyte-centered mechanism underlying NOD1-mediated atrial dysfunction, and the contribution of non-myocyte cell populations remains to be defined.

Beyond these structural alterations, proteomic, and molecular analyses revealed that NOD1 deficiency preserved the expression of key Ca^{2+}-handling proteins, including SERCA2a

and RyR2, in TAC-subjected mice. This preservation resulted in normalized SR Ca^{2+} reuptake, Ca^{2+} transient amplitude, and SR Ca^{2+} load, translating into improved atrial Ca^{2+} cycling and contractile performance. Importantly, pharmacological NOD1 inhibition using ML-130 reproduced the protective effects observed in *Nod1*$^{-/-}$ mice, preventing both TAC-induced Ca^{2+} mishandling and atrial hypertrophy, thereby strengthening the implication of NOD1 signaling in atrial remodeling.

At the post-translational level, NOD1 deficiency further prevented pathological signaling remodeling [26–29]. Phosphoproteomic profiling revealed global hyperphosphorylation in WT-TAC atria, with RyR2 emerging as a major phosphorylation hub. Critically, NOD1 deficiency prevented CaMKII-mediated hyperphosphorylation of RyR2 at Ser2814, the principal CaMKII target site. This selective prevention of CaMKII-dependent RyR2 phosphorylation markedly reduced diastolic Ca^{2+} leak, a critical driver of atrial dysfunction and enlargement [30].

RyR2 phosphorylation is tightly regulated by a balance of kinases and phosphatases [26–29]. Consistent with increased RyR2 phosphorylation in WT-TAC atria, we observed reduced expression of the phosphatase regulatory subunit PP1R3A, whose downregulation has been associated with increased RyR2 phosphorylation and SR Ca^{2+} leak [28]. NOD1 deficiency prevented PP1R3A downregulation, reinforcing the protective role of NOD1 deficiency in HF-associated atrial myopathy.

Pathological diastolic SR Ca^{2+} leak in WT-TAC atrial myocytes contributes to atrial dysfunction and enlargement [21,31]. Beyond excitation-contraction coupling, aberrant Ca^{2+} signaling activates Ca^{2+}-sensitive transcriptional programs, including CaMKII-dependent pathways that promote maladaptive remodeling [32]. Accordingly, the absence of atrial hypertrophy in *Nod1*$^{-/-}$-TAC mice is consistent with normalized Ca^{2+} handling and reduced

CaMKII activation. These findings align with prior evidence showing that pathological SR Ca^{2+} leak accelerates maladaptive remodeling and HF progression under pressure overload [33].

The pathogenic role of NOD1 in atrial Ca^{2+} dysregulation was further validated through gain-of-function studies. Acute administration of the selective NOD1 agonist C12-iE-DAP in WT mice induced Ca^{2+}-handling abnormalities closely resembling those observed in the TAC mouse model, including impaired systolic Ca^{2+} release, reduced SR Ca^{2+} load, and increased RyR2-mediated diastolic Ca^{2+} leak. These effects were abolished by pharmacological CaMKII inhibition with KN-93, establishing strict dependence on CaMKII activation. Importantly, *RyR2*-S2814A mice (phosphorylation-deficient at Ser2814) were protected from NOD1-driven Ca^{2+} mishandling, identifying CaMKII-dependent RyR2-Ser2814 phosphorylation as the critical mechanistic node linking NOD1 activation to atrial Ca^{2+} dysregulation. Importantly, AF inducibility was not significantly increased following acute NOD1 activation, in line with the data obtained from patients and the LAI-AF swine model.

These findings uncover the NOD1–CaMKII–RyR2 axis as a cardiomyocyte-centered pathway linking innate immune activation to atrial Ca^{2+} mishandling, in line with recent reports implicating IL-1β-NLRP3 signaling in CaMKII-dependent RyR2 hyperphosphorylation and pathological Ca^{2+} leak in human atrial cardiomyocytes [14]. The translational relevance of this mechanistic framework is directly supported by molecular analyses of human HF atrial myocardium, which revealed enrichment of inflammatory and Ca^{2+} signaling pathways, together with increased CaMKII phosphorylation at Thr-286/287, indicating that CaMKII hyperactivation is a conserved feature of the failing human atrium and that the NOD1–CaMKII–RyR2 axis identified in experimental models operates in the clinical setting.

Collectively, these findings position NOD1 as a molecular mediator of HF–associated atrial myopathy, with potential applications in both patient stratification and mechanism-based intervention. From a diagnostic standpoint, atrial NOD1 expression correlated with established indices of atrial disease severity across divergent ventricular phenotypes and irrespective of documented rhythm status, supporting NOD1 pathway activation as a molecular signature of atrial remodeling burden that may refine patient stratification beyond conventional clinical parameters. From a therapeutic standpoint, both genetic deletion and pharmacological inhibition of NOD1 attenuated atrial Ca^{2+} dysregulation and structural remodeling, providing convergent preclinical evidence for NOD1 targeted intervention. Mechanistically, the identification of CaMKII-dependent RyR2-Ser2814 phosphorylation as the critical downstream effector defines a therapeutically actionable axis, positioning the NOD1–CaMKII–RyR2 pathway as a tractable multi-level target for intervention. Together, these findings establish a framework for the development of clinically applicable strategies to both monitor and modulate NOD1 pathway activity in HF-associated atrial myopathy.

Limitations

Several limitations of the present study warrant consideration. Rhythm classification in the human cohort was based on standard 12-lead electrocardiography and systematic review of clinical records, without continuous ambulatory monitoring; accordingly, a proportion of patients categorized as sinus rhythm may have had undetected paroxysmal AF. An analogous consideration applies to the porcine LAI model, in which continuous rhythm monitoring was available in the AF subgroup through implanted devices, but not in the sinus rhythm subgroup; therefore, low-burden or transient atrial arrhythmias cannot be fully excluded in these animals. Future studies incorporating prolonged rhythm monitoring will enable more precise characterization of the relationship between NOD1 expression and AF burden. Although the present study primarily supports a cardiomyocyte-centered mechanism, the contribution of

non-myocyte cell populations, including fibroblasts and endothelial cells, to NOD1-mediated atrial remodeling remains to be defined and warrants further investigation.

Conclusions

This study identifies NOD1 as a previously unrecognized contributor to HF-associated atrial myopathy, acting through a cardiomyocyte-centered inflammatory pathway that converges on CaMKII-dependent RyR2 hyperphosphorylation and pathological Ca^{2+} mishandling. The correlation of atrial NOD1 expression with structural and functional indices of disease severity, together with the preclinical efficacy of NOD1 blockade, establishes the NOD1–CaMKII–RyR2 axis as both a molecular indicator of atrial remodeling burden and a mechanism-based therapeutic target in HF-associated atrial myopathy.

Abbreviations

AF: atrial fibrillation; AoB: aortic banding; BW: body weight; CaMKII: Ca^{2+}/calmodulin-dependent protein kinase II; CMR: cardiac magnetic resonance; DAMPs: damage-associated molecular patterns; E/E′: ratio of early mitral inflow velocity to early mitral annular velocity; FDR: false discovery rate; GAPDH: glyceraldehyde-3-phosphate dehydrogenase; HF: heart failure; HFmrEF: heart failure with mildly reduced ejection fraction; HFrEF: heart failure with reduced ejection fraction; HW: heart weight; IHC: immunohistochemistry; IL1B: interleukin 1 beta; IL6: interleukin 6; LA: left atrium; LAI: left atrial infarction; LAW: left atrial weight; LV: left ventricle; LVEF: left ventricular ejection fraction; LVEDV: left ventricular end-diastolic volume; LVESV: left ventricular end-systolic volume; NF: non-failing; NLRs: NOD-like receptors; NOD1: nucleotide-binding oligomerization domain-containing protein 1; NT-proBNP: N-terminal pro-B-type natriuretic peptide; NYHA: New York Heart Association; PAMPs: pathogen-associated molecular patterns; PASP: pulmonary artery systolic pressure; PP1: protein phosphatase 1; PRRs: pattern recognition receptors; RA: right atrium; RAW: right

atrial weight; RIP2: receptor-interacting serine/threonine-protein kinase 2; RyR2: ryanodine receptor 2; SERCA2a: sarco/endoplasmic reticulum Ca^{2+}-ATPase 2a; SR: sarcoplasmic reticulum; TAC: transverse aortic constriction; TL: tibia length; TRPG: tricuspid regurgitation peak gradient; WT: wild-type.

Supplementary Material

Supplementary Methods, Figures and Tables.

Acknowledgments

The authors thank Gabriel Núñez (University of Michigan, USA) for kindly providing the *Nod1*$^{-/-}$ mice. We also thank Carlota Largo Aramburu, Laura Martin Nunez, Mónica Martín Belinchon, Teresa Navarro Hernanz, and María Rodriguez Martinez for technical assistance. We also thank Emiliano Medei (Federal University of Rio de Janeiro, Brazil) for his scientific advice and insightful discussions.

Funding

This work was supported by the Spanish Ministry of Economy and Competitiveness and the European Regional Development Fund (SAF-2017-84777R), Instituto de Salud Carlos III (ISCIII) (PI20/01482 and PI23/01014; F21/00259, CM23/00121, CD22/00055, PMP 22/00098, PT23/00028), Ministry of Science and Innovation (CNS2023-145161). Spanish Society of Cardiology, Translational Project 2019 and Heart Rhythm Association (SEC, España), Proyecto Asociación Insuficiencia Cardiaca (Trasplante Cardiaco) 2020, European Regional Development Fund, European Social Fund, and CIBERCV, a network funded by ISCIII, Spanish Ministry of Science, Innovation and Universities. RED2022-134511-T Research Network. Ministry of Science and Innovation. This study was also supported by competitive grants PID2021-122348NB-I00 funded by MICIU/AEI/ 10.13039/501100011033 and by "ERDF A way of making Europe", PLEC2022-009298, PLEC2022-009235 and

EQC2021-007053-P funded by MICIU/AEI/10.13039/501100011033 and by "European Union NextGenerationEU/ PRTR", and S2022/B-7333-CM (INMUNOVAR-CM) funded by Comunidad de Madrid. The project leading to these results has received funding from "la Caixa" Foundation under the project code LCF/PR/HR22/52420019. The CNIC is supported by the Instituto de Salud Carlos III (ISCIII), the Ministry of Science, University and Innovation (MICIU) and the Pro CNIC Foundation), and is a Severo Ochoa Center of Excellence (grant CEX2020-001041-S funded by MICIU/AEI/10.13039/501100011033).

Author contributions

MGF, AVB, ABS, and PCP designed and performed experiments, acquired and analyzed data, and contributed to manuscript writing. The order of the co–first authors was assigned based on overall contribution to experimental work and data analysis. CGA, BI, DFD and JJ designed, performed, and analyzed the porcine models of atrial remodeling. IJ and JV performed and analyzed proteomic and phosphoproteomic experiments. AA, TLF, RP, AAroca, MAR, RM, BRS, and JN contributed to patient recruitment, clinical data acquisition, and interpretation of human studies. YAS, SKL, JANG, and JAB contributed to mouse studies, pharmacological experiments, and Ca^{2+} handling analyses. MT, ELC, TS, AO, and PP provided technical support, reagents, and methodological expertise. GRH, CD, LB, XHTW, and MFV supervised the study, secured funding, and provided critical intellectual input. MGF and MFV wrote the manuscript with input from all authors. All authors reviewed and approved the final manuscript.

Data availability

The raw proteomics data have been deposited in the jPOST repository (accession: **JPST003217,** key **6433)**. Raw data from RNA-Seq data have been deposited in the European Nucleotide Archive (ENA, EMBL-EBI) under accession number **PRJEB107793** and will be

584 released upon publication. Additional data supporting the findings of this study are available
585 from the corresponding author upon reasonable request.

586 **Competing Interests**

587 The authors have declared that no competing interests exist.

588 **References**

589 1. Shahim B, Kapelios CJ, Savarese G, Lund LH. Global public health burden of heart failure:
590 an updated review. Card Fail Rev. 2023; 9: e11.

591 2. Frantz S, Hundertmark MJ, Schulz-Menger J, Bengel FM, Bauersachs J. Left ventricular
592 remodelling post-myocardial infarction: pathophysiology, imaging, and novel therapies. Eur
593 Heart J. 2022; 43: 2549–61.

594 3. Konstam MA, Kramer DG, Patel AR, Maron MS, Udelson JE. Left ventricular remodeling
595 in heart failure: current concepts in clinical significance and assessment. JACC Cardiovasc
596 Imaging. 2011; 4: 98–108.

597 4. Shen MJ, Arora R, Jalife J. Atrial myopathy. JACC Basic Transl Sci. 2019; 4: 640–54.

598 5. Dobrev D, Aguilar M, Heijman J, Guichard J-B, Nattel S. Postoperative atrial fibrillation:
599 mechanisms, manifestations and management. Nat Rev Cardiol. 2019; 16: 417–36.

600 6. Nattel S, Heijman J, Zhou L, Dobrev D. Molecular basis of atrial fibrillation pathophysiology
601 and therapy: a translational perspective. Circ Res. 2020; 127: 51–72.

602 7. Hohendanner F, Messroghli D, Bode D, et al. Atrial remodelling in heart failure: recent
603 developments and relevance for heart failure with preserved ejection fraction. ESC Heart Fail.
604 2018; 5: 211–21.

8. Hoit BD. Left atrial reservoir strain: its time has come. JACC Cardiovasc Imaging. 2022; 15: 392–4.

9. Tastet L, Lim LJ, Bibby D, et al. Primary atriopathy in mitral valve prolapse: echocardiographic evidence and clinical implications. Circ Cardiovasc Imaging. 2024; 17: e016319.

10. Zhang MJ, Ji Y, Wang W, et al. Association of atrial fibrillation with stroke and dementia accounting for left atrial function and size. JACC Adv. 2023; 2: 100408.

11. Ridker PM. Anticytokine agents: targeting interleukin signaling pathways for the treatment of atherothrombosis. Circ Res. 2019; 124: 437–50.

12. Theall B, Alcaide P. The heart under pressure: immune cells in fibrotic remodeling. Curr Opin Physiol. 2022; 25: 100484.

13. Jaén RI, Val-Blasco A, Prieto P, et al. Innate immune receptors, key actors in cardiovascular diseases. JACC Basic Transl Sci. 2020; 5: 735–49.

14. Heijman J, Muna AP, Veleva T, et al. Atrial myocyte NLRP3/CaMKII nexus forms a substrate for post-operative atrial fibrillation. Circ Res. 2020; 127: 1036–55.

15. Li N, Chiang DY, Wang S, et al. Ryanodine receptor-mediated calcium leak drives progressive development of an atrial fibrillation substrate in a transgenic mouse model. Circulation. 2014; 129: 1276–85.

16. Yao C, Veleva T, Scott L, et al. Enhanced cardiomyocyte NLRP3 inflammasome signaling promotes atrial fibrillation. Circulation. 2018; 138: 2227–42.

17. Delgado C, Ruiz-Hurtado G, Gómez-Hurtado N, et al. NOD1, a new player in cardiac function and calcium handling. Cardiovasc Res. 2015; 106: 375–86.

627 18. Lin HB, Naito K, Oh Y, et al. Innate immune Nod1/RIP2 signaling is essential for cardiac
628 hypertrophy but requires mitochondrial antiviral signaling protein for signal transductions and
629 energy balance. Circulation. 2020; 142: 2240–58.

630 19. Mann DL. Innate immunity and the failing heart. Circ Res. 2015; 116: 1254–68.

631 20. Dobrev D, Heijman J, Hiram R, Li N, Nattel S. Inflammatory signalling in atrial
632 cardiomyocytes: a novel unifying principle in atrial fibrillation pathophysiology. Nat Rev
633 Cardiol. 2022; 20: 145–67.

634 21. Nattel S, Burstein B, Dobrev D. Atrial remodeling and atrial fibrillation: mechanisms and
635 implications. Circ Arrhythm Electrophysiol. 2008; 1: 62–73.

636 22. Yang H, Zhu J, Fu H, Shuai W. Dapansutrile ameliorates atrial inflammation and
637 vulnerability to atrial fibrillation in HFpEF rats. Heart Lung Circ. 2024; 33: 65–77.

638 23. Modin D, Sengeløv M, Jørgensen PG, et al. Prognostic value of left atrial functional
639 measures in heart failure with reduced ejection fraction. J Card Fail. 2019; 25: 87–96.

640 24. Carluccio E, Biagioli P, Mengoni A, et al. Left atrial reservoir function and outcome in
641 heart failure with reduced ejection fraction. Circ Cardiovasc Imaging. 2018; 11: e007696.

642 25. Joglar JA, Chung MK, Armbruster AL, et al. 2023 ACC/AHA/ACCP/HRS guideline for
643 the diagnosis and management of atrial fibrillation: a report of the American College of
644 Cardiology/American Heart Association Joint Committee on Clinical Practice Guidelines.
645 Circulation. 2024; 149: e1–e156.

646 26. Wehrens XHT, Lehnart SE, Reiken SR, Marks AR. Ca^{2+}/calmodulin-dependent protein
647 kinase II phosphorylation regulates the cardiac ryanodine receptor. Circ Res. 2004; 94: e61–
648 e70.

649 27. Wehrens XHT, Lehnart SE, Marks AR. Intracellular calcium release and cardiac disease.
650 Annu Rev Physiol. 2005; 67: 69–98.

651 28. Alsina KM, Hulsurkar M, Brandenburg S, et al. Loss of protein phosphatase 1 regulatory
652 subunit PPP1R3A promotes atrial fibrillation. Circulation. 2019; 140: 681–93.

653 29. Vest JA, Wehrens XHT, Reiken SR, et al. Defective cardiac ryanodine receptor regulation
654 during atrial fibrillation. Circulation. 2005; 111: 2025–32.

655 30. Ling H, Zhang T, Pereira L, et al. Requirement for Ca^{2+}/calmodulin-dependent kinase II in
656 the transition from pressure overload-induced cardiac hypertrophy to heart failure in mice. J
657 Clin Invest. 2009; 119: 1230–40.

658 31. Yeh YH, Wakili R, Qi XY, et al. Calcium-handling abnormalities underlying atrial
659 arrhythmogenesis and contractile dysfunction in dogs with congestive heart failure. Circ
660 Arrhythm Electrophysiol. 2008; 1: 93–102.

661 32. Akazawa H, Komuro I. Roles of cardiac transcription factors in cardiac hypertrophy. Circ
662 Res. 2003; 92: 1079–88.

663 33. Van Oort RJ, Respress JL, Li N, et al. Accelerated development of pressure overload-
664 induced cardiac hypertrophy and dysfunction in an RyR2-R176Q knockin mouse model.
665 Hypertension. 2010; 55: 932–8.

666

667

668

669

670

Tables

Table 1. Baseline characteristics of non-failing (NF) and heart failure (HF) patients.

Data are mean ± SEM or %; statistical analyses performed by unpaired t-test or $\chi 2$ test ($P < 0.05$ considered significant).

	NF n = 42	HF n = 36	*P* value
Demographics			
Age (years)	61.83 ± 1.87	65.58 ± 1.62	0.140
Female (%)	30.95	25.00	0.620
Clinical profile			
Body mass index (kg/m^2)	27.63 ± 0.69	26.68 ± 0.79	0.288
Diabetes mellitus (%)	14.29	27.78	0.168
Hypertension (%)	57.14	61.11	0.819
Dyslipidemia (%)	57.14	52.78	0.820
Functional classification			
NYHA III/IV (%)	0	25.00	<0.001
Medication use			
Diuretics (%)	21.62	65.63	<0.001
Angiotensin-converting enzyme inhibitors (%)	40.54	34.38	0.628
Angiotensin receptor blockers (%)	21.62	25.00	0.781
Beta-adrenergic blockers (%)	38.24	62.50	0.084
Laboratory measurements			
Creatinine (mg/dL)	0.89 ± 0.03	1.02 ± 0.07	0.066
Hemoglobin (g/dL)	14.33 ± 0.20	13.97 ± 0.23	0.245
C-reactive protein (mg/L)	2.73 ± 0.37	3.76 ± 0.76	0.209
Creatinine clearance (mL/min)	82.05 ± 1.70	73.16 ± 3.03	0.010
Echocardiographic parameters			
Indexed LVEDV (mL/m^2)	49.90 ± 3.02	65.32 ± 6.92	0.035
Indexed LVESV (mL/m^2)	17.65 ± 1.51	35.98 ± 4.09	<0.001
PASP (mmHg)	23.25 ± 2.93	34.56 ± 2.83	0.030
Maximum TRPG (mmHg)	10.75 ± 2.65	25.73 ± 2.62	0.005
Lateral E/E′ ratio	10.28 ± 1.08	16.71 ± 3.40	0.043

E/E′, ratio of early mitral inflow velocity (E) to early diastolic mitral annular velocity (E′) by tissue Doppler; LVEDV, left ventricular end-diastolic volume; LVESV, left ventricular end-systolic volume; NYHA, New York Heart Association; PASP, pulmonary artery systolic pressure; TRPG, tricuspid regurgitation peak gradient.

Table 2. Cardiac magnetic resonance-derived ventricular parameters in Control and AoB Yucatan minipigs.

Data are mean ± SEM; statistical analyses performed by unpaired t-test ($P < 0.05$ considered significant).

	Control n = 17	AoB n = 13	*P* value
Body measurements			
Body weight (kg)	71.24 ± 3.05	84.88 ± 9.82	0.003
Body mass index (kg/m^2)	1.439 ± 0.04	1.611 ± 0.03	0.003
Cardiac magnetic resonance parameters			
Heart rate (bpm)	70.18 ± 4.33	79.00 ± 7.06	0.273
LV mass (g)	63.70 ± 3.65	95.05 ± 7.62	0.001
Indexed LV mass (g/m^2)	53.21 ± 3.83	58.78 ± 4.15	0.335
LV wall thickness (mm)	10.43 ± 0.73	10.98 ± 0.76	0.613
Indexed LV wall thickness (mm/m^2)	7.38 ± 0.62	6.96 ± 0.51	0.609
LVED diameter (mm)	44.15 ± 1.45	46.42 ± 1.50	0.290
Indexed LVED diameter (mm/m^2)	31.04 ± 1.28	29.33 ± 0.93	0.278
LVES diameter (mm)	29.90 ± 1.52	27.71 ± 1.60	0.333
Indexed LVES diameter (mm/m^2)	20.71 ± 1.17	18.60 ± 0.69	0.111
LVEDV (mL)	96.18 ± 7.09	99.94 ± 10.11	0.756
Indexed LVEDV (mL/m²)	66.74 ± 4.27	61.45 ± 5.44	0.444
LVESV (mL)	36.59 ± 3.81	22.84 ± 2.83	0.014
Indexed LVESV (mL/m²)	25.40 ± 2.37	14.36 ± 1.76	0.002

LVED, left ventricular end-diastolic; LVEDV, left ventricular end-diastolic volume; LVES, left ventricular end-systolic; LVESV, left ventricular end-systolic volume.

Table 3. Cardiac magnetic resonance-derived ventricular parameters in Control and LAI Large White pigs.

Data are mean ± SEM; statistical analyses performed by unpaired t-test ($P < 0.05$ considered significant).

	Control n = 14	LAI n = 21	*P* value
Body measurements			
Body weight (kg)	66.36 ± 3.93	59.45 ± 2.11	0.102
Body mass index (kg/m^2)	1.37 ± 0.05	1.284 ± 0.03	0.121
Cardiac magnetic resonance parameters			
Heart rate (bpm)	73.71 ± 3.49	69.05 ± 4.08	0.424
LV mass (g)	70.04 ± 4.34	82.13 ± 3.25	0.031
Indexed LV mass (g/m^2)	53.01 ± 2.8	64.05 ± 2.13	0.002
LV wall thickness (mm)	7.52 ± 0.35	9.88 ± 0.87	0.046
Indexed LV wall thickness (mm/m^2)	5.56 ± 0.33	7.88 ± 0.78	0.031
LVED diameter (mm)	51.28 ± 1.86	64.37 ± 1.82	<0.001
Indexed LVED diameter (mm/m^2)	37.59 ± 1.09	50.66 ± 1.80	<0.001
LVES diameter (mm)	35.29 ± 1.23	50.17 ± 1.63	<0.001
Indexed LVES diameter (mm/m^2)	28.15 ± 1.81	40.41 ± 2.38	<0.001
LVEDV (mL)	121.70 ± 8.53	179.80 ± 8.09	<0.001
Indexed LVEDV (mL/m²)	87.65 ± 4.16	140.20 ± 5.47	<0.001
LVESV (mL)	45.86 ± 4.01	104.00 ± 6.23	<0.001
Indexed LVESV (mL/m²)	32.91 ± 2.30	81.13 ± 4.42	<0.001

LVED, left ventricular end-diastolic; LVEDV, left ventricular end-diastolic volume; LVES, left ventricular end-systolic; LVESV, left ventricular end-systolic volume.

Table 4. Macroscopic and cardiac magnetic resonance-derived ventricular parameters in WT and *Nod1*$^{-/-}$-Sham and TAC mice.

Data are mean ± SEM; statistical analyses performed by ANOVA with Tukey's post hoc ($P < 0.05$ considered significant). * $P < 0.05$, ** $P < 0.01$, *** $P < 0.001$ *vs*. WT-Sham; $^{\#}$ $P < 0.05$, $^{\#\#}$ $P < 0.01$, $^{\#\#\#}$ $P < 0.001$ *vs*. WT-TAC; $^{\&\&\&}$ $P < 0.001$ *vs*. *Nod1*$^{-/-}$-Sham.

	WT-Sham n = 15	WT-TAC n = 17	*Nod1*$^{-/-}$-Sham n = 16	*Nod1*$^{-/-}$-TAC n = 18
Body parameters				
BW (g)	27.88 ± 0.51	28.88 ± 0.58	27.82 ± 0.44	28.08 ± 0.68
TL (mm)	17.18 ± 0.10	17.25 ± 0.11	17.30 ± 0.10	17.10 ± 0.12
HW (mg)	178.3 ± 4.22	313.30 ± 9.48***	174.30 ± 3.54$^{\#\#\#}$	221.50 ± 8.49***$^{, \#\#\#, \&\&\&}$
LAW (mg)	6.393 ± 0.28	21.76 ± 0.92***	5.33 ± 0.26$^{\#\#\#}$	7.51 ± 0.39$^{\#\#\#}$
RAW (mg)	6.47 ± 0.43	10.51 ± 0.70***	5.54 ± 0.26$^{\#\#\#}$	5.92 ± 0.39$^{\#\#\#}$
HW/BW (mg/g)	6.40 ± 0.14	10.94 ± 0.43***	6.28 ± 0.12$^{\#\#\#}$	7.89 ± 0.24**$^{, \#\#\#, \&\&\&}$
LAW/BW (mg/g)	0.23 ± 0.01	0.76 ± 0.04***	0.19 ± 0.01$^{\#\#\#}$	0.27 ± 0.03$^{\#\#\#}$
RAW/BW (mg/g)	0.23 ± 0.01	0.37 ± 0.03***	0.20 ± 0.01$^{\#\#\#}$	0.21 ± 0.01$^{\#\#\#}$
HW/TL (mg/mm)	10.38 ± 0.23	18.20 ± 0.61***	10.08 ± 0.20$^{\#\#\#}$	12.95 ± 0.48***$^{, \#\#\#, \&\&\&}$
LAW/TL (mg/mm)	0.37 ± 0.01	1.27 ± 0.06***	0.31 ± 0.02$^{\#\#\#}$	0.44 ± 0.04$^{\#\#\#}$
RAW/TL (mg/mm)	0.38 ± 0.02	0.62 ± 0.04***	0.32 ± 0.01$^{\#\#\#}$	0.35 ± 0.02$^{\#\#\#}$
Cardiac magnetic resonance parameters				
Heart rate (bpm)	439.3 ± 13.93	465.6 ± 12.93	430.9 ± 17.93	464.5 ± 30.95
LV mass (mg)	76.08 ± 1.69	104.50 ± 4.59***	66.94 ± 2.99$^{\#\#\#}$	86.11 ± 3.31$^{\#\#, \&\&\&}$
LV wall thickness (mm)	0.89 ± 0.02	1.27 ± 0.02***	0.97 ± 0.02$^{\#\#\#}$	1.04 ± 0.02***$^{, \#\#\#}$
LVED diameter (mm)	3.86 ± 0.07	4.54 ± 0.06***	3.94 ± 0.10$^{\#\#\#}$	4.06 ± 0.10$^{\#\#\#}$
LVES diameter (mm)	2.39 ± 0.05	3.39 ± 0.10***	2.60 ± 0.08$^{\#\#\#}$	2.94 ± 0.11***$^{, \#\#}$
LVEDV (µL)	35.80 ± 1.28	50.23 ± 2.64**	33.41 ± 2.34$^{\#\#\#}$	39.92 ± 2.92$^{\#}$
LVESV (µL)	10.63 ± 0.95	25.58 ± 2.59***	12.19 ± 1.17$^{\#\#\#}$	18.33 ± 2.27*$^{, \#}$

BW, body weight; HW, heart weight; LAW, left atrial weight; LVED, left ventricular end-diastolic; LVEDV, left ventricular end-diastolic volume; LVES, left ventricular end-systolic; LVESV, left ventricular end-systolic volume; RAW, right atrial weight; TL, tibia length.

Figures

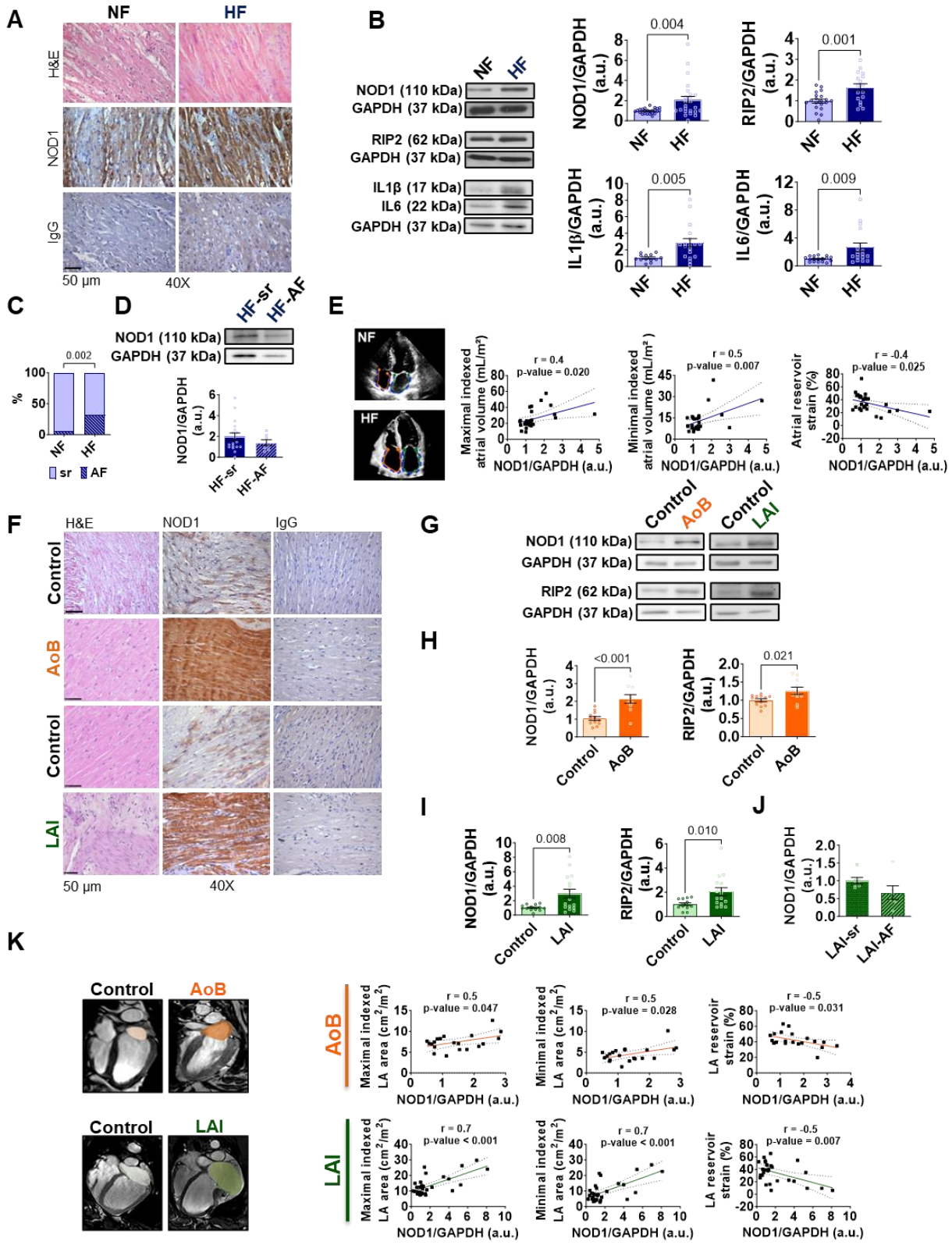
A
NF
HF
H&E
NOD1
IgG
50 µm
40X
B
NF
HF
NOD1 (110 kDa)
GAPDH (37 kDa)
RIP2 (62 kDa)
GAPDH (37 kDa)
IL1β (17 kDa)
IL6 (22 kDa)
GAPDH (37 kDa)
NOD1/GAPDH (a.u.)
0.004
RIP2/GAPDH (a.u.)
0.001
IL1β/GAPDH (a.u.)
0.005
IL6/GAPDH (a.u.)
0.009
C
0.002
%
sr
AF
D
HF-sr
HF-AF
NOD1 (110 kDa)
GAPDH (37 kDa)
NOD1/GAPDH (a.u.)
E
NF
HF
Maximal indexed atrial volume (mL/m²)
r = 0.4
p-value = 0.020
Minimal indexed atrial volume (mL/m²)
r = 0.5
p-value = 0.007
Atrial reservoir strain (%)
r = -0.4
p-value = 0.025
NOD1/GAPDH (a.u.)
F
H&E
NOD1
IgG
Control
AoB
Control
LAI
50 µm
40X
G
Control
AoB
Control
LAI
NOD1 (110 kDa)
GAPDH (37 kDa)
RIP2 (62 kDa)
GAPDH (37 kDa)
H
NOD1/GAPDH (a.u.)
<0.001
RIP2/GAPDH (a.u.)
0.021
Control
AoB
I
NOD1/GAPDH (a.u.)
0.008
RIP2/GAPDH (a.u.)
0.010
Control
LAI
J
NOD1/GAPDH (a.u.)
LAI-sr
LAI-AF
K
Control
AoB
Control
LAI
AoB
LAI
Maximal indexed LA area (cm²/m²)
r = 0.5
p-value = 0.047
Minimal indexed LA area (cm²/m²)
r = 0.5
p-value = 0.028
LA reservoir strain (%)
r = -0.5
p-value = 0.031
r = 0.7
p-value < 0.001
r = 0.7
p-value < 0.001
r = -0.5
p-value = 0.007
NOD1/GAPDH (a.u.)

Figure 1. NOD1 signaling is upregulated in atrial myocardium of patients and swine models of heart failure. (A) Representative hematoxylin-eosin (H&E) and immunohistochemical (IHC) staining for NOD1 in atrial tissue, with isotype controls from non-failing (NF) and heart failure (HF) patients. (B) Western blot and quantification of NOD1 (NF, n = 24; HF, n = 25), its adaptor RIP2 (NF, n = 20; HF, n = 17), IL-1β (NF, n = 13; HF, n = 18), and IL6 (NF, n = 17; HF, n = 18) expression in atrial tissue, normalized to GAPDH. (C) Prevalence of AF (%) in both groups. (D) Subgroup comparison of NOD1 protein levels in HF patients in sinus rhythm (HF-SR, n = 18) and atrial fibrillation (HF-AF, n = 7). (E) Representative echocardiographic images and correlations between atrial NOD1 protein levels and maximal and minimal atrial volumes and reservoir strain (NF, n = 29; HF, n = 26). (F) Representative H&E, NOD1 IHC staining and isotype controls obtained in LA tissue from aortic banding (AoB) and left-atrial infarction (LAI) porcine models and Control animals. (G-I) Western blot and quantification of NOD1 and its adaptor RIP2 expression in left atrial (LA) tissue from (G-H) Control (n = 12) and AoB (n = 10) Yucatan minipigs and from (G-I) Control (n = 13) and LAI (n = 16) Large White Pigs, normalized to GAPDH. (J) Quantification of NOD1 protein levels in atrial tissue from a separate cohort of LAI animals (LAI-sr, n = 6 and LAI-AF, n = 6), normalized to GAPDH. (K) Representative cardiac magnetic resonance (CMR) images and correlations between LA NOD1 expression and atrial area and reservoir strain. Data are mean ± SEM; statistical analyses performed by unpaired t-test or Pearson's correlation ($P < 0.05$ considered significant).

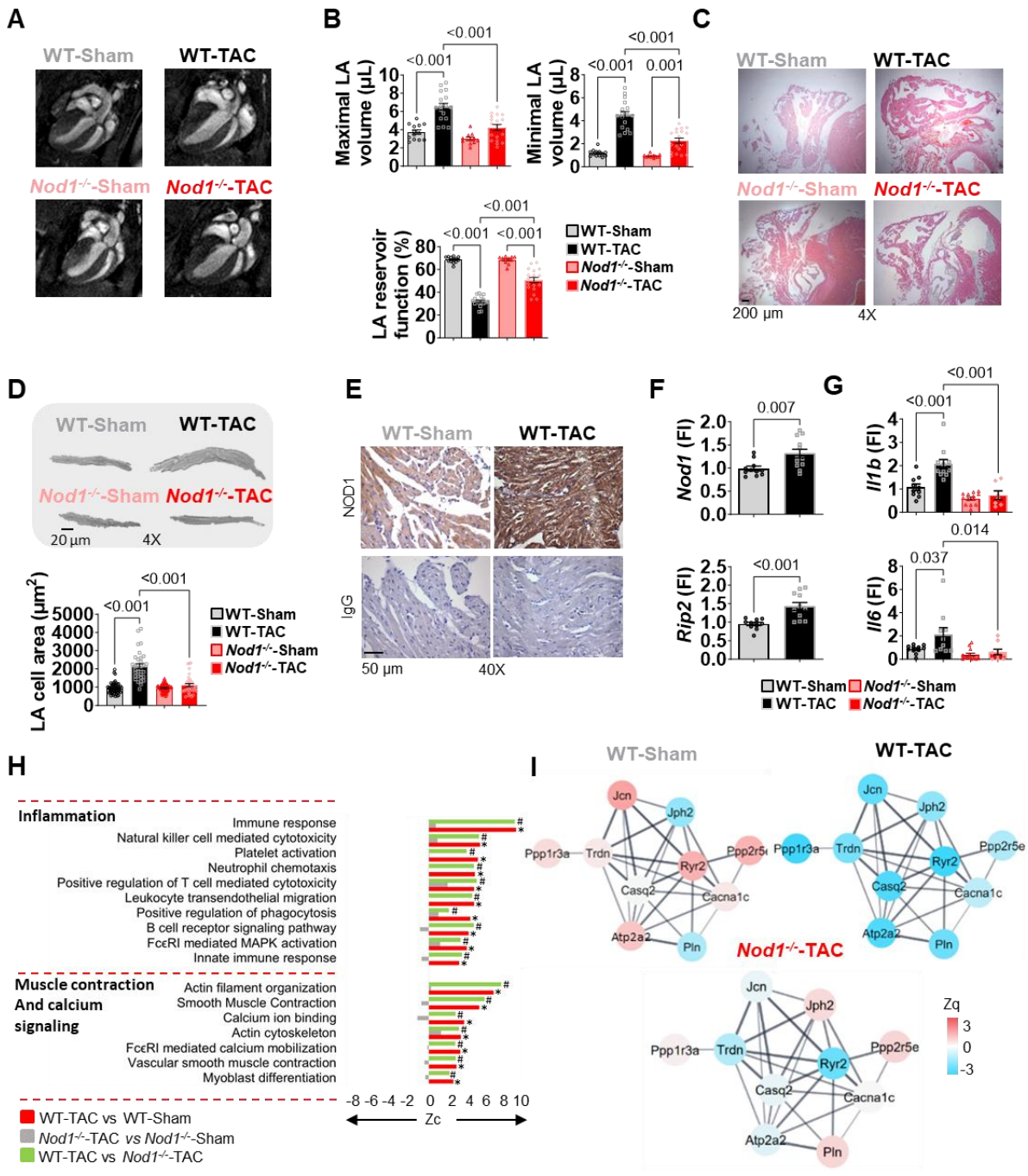

Figure 2. NOD1 deficiency prevents atrial remodeling and proteomic alterations in mice subjected to pressure overload. (A) Representative long-axis four-chamber CMR images illustrating differences in left atrial size across groups. (B) Maximal and minimal LA volumes and reservoir function obtained in WT-Sham (n = 13), WT-TAC (n = 17), *Nod1*$^{-/-}$-Sham (n = 11) and *Nod1*$^{-/-}$*-TAC* (n = 18). (C) Representative H&E staining illustrating atrial remodeling in all groups. (D) Representative images and quantification of LA cardiomyocyte cross-

sectional area in WT-Sham (*n* = 57cells/6 mice), WT-TAC (*n* = 33 cells/5 mice), *Nod1*$^{-/-}$-Sham (*n* = 53 cells/3 mice) and *Nod1*$^{-/-}$*-TAC* (*n* = 35 cells/6 mice). (E) Representative IHC staining for NOD1 in LA tissue, with isotype controls. (F) LA mRNA expression of *Nod1* and *Rip2* normalized to 36B4 and relative to WT-Sham. (G) LA mRNA expression of *Il1b* and *Il6* normalized to 36B4 and relative to WT-Sham. (H) Functional enrichment analysis of murine LA tissue showing differential enrichment of inflammation- and Ca^{2+}-related pathways across the indicated comparisons. Bar plots represent differential pathway enrichment for the following comparisons (n = 4 per group). Zc values represent $\log_2$ fold-change standardized to units of standard deviation. Significant differences noted at FDR<0.05 (*WT-TAC vs. WT-Sham. #WT-TAC vs. *Nod1*$^{-/-}$-TAC). (I) STRING protein-protein interaction network of differentially expressed Ca^{2+} handling proteins. Data are mean ± SEM; statistical analyses performed by ANOVA with Tukey's post hoc, nested ANOVA or unpaired t-test ($P < 0.05$ considered significant).

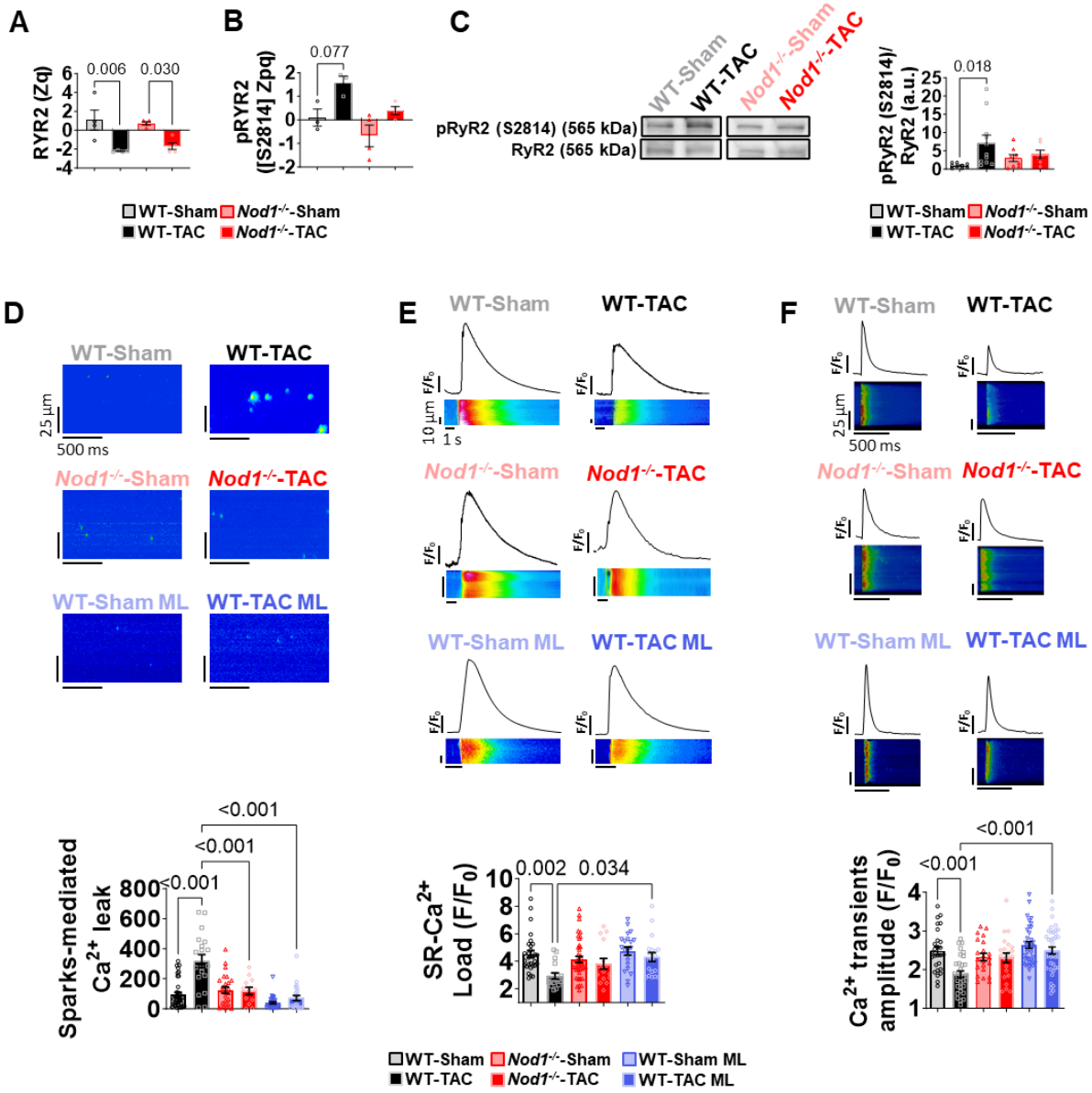

779

780 **Figure 3. NOD1 deficiency or pharmacological inhibition prevents TAC-induced**
781 **intracellular Ca^{2+} dysregulation.** WT-Sham and WT-TAC mice were treated with the
782 selective NOD1 inhibitor ML-130 (ML; 2 mg/kg, i.p., every other day for 4 weeks). (A-B)
783 Quantification of RyR2 protein abundance (A; Zq values, $\log_2$ fold-change relative to WT-
784 Sham) and RyR2 phosphorylation at Ser2814 (B; Zpq values). Zpq values represent $\log_2$ fold-
785 change standardized to units of standard deviation. (C) Western blot validation of RyR2
786 phosphorylation at Ser2814 in LA tissue, normalized to total RyR2 (WT-Sham, n = 9; WT-
787 TAC, n = 11; *Nod1*$^{-/-}$-Sham, n = 8; *Nod1*$^{-/-}$-TAC, n = 7). (D-F) Representative confocal line-

788 scan images and quantification of (D) sparks-mediated Ca^{2+} leak indicating diastolic Ca^{2+} leak
789 in quiescent cardiomyocytes, (E) caffeine-evoked Ca^{2+} transients reflecting sarcoplasmic
790 reticulum (SR) Ca^{2+} load and (F) electrically evoked Ca^{2+} transients in LA cardiomyocytes
791 from WT-Sham (n = 27-41 cells/6 mice), WT-TAC (n = 19-31 cells/5 mice), *Nod1*$^{-/-}$-Sham (n
792 = 22-42 cells/3 mice), *Nod1*$^{-/-}$*-TAC* (n = 12-22 cells/6 mice), WT-Sham ML (n = 21-39 cells/3
793 mice), and WT-TAC ML (n = 22-40 cells/3 mice). Data are mean ± SEM; statistical analyses
794 performed by ANOVA with Tukey's post hoc or nested ANOVA ($P < 0.05$ considered
795 significant).

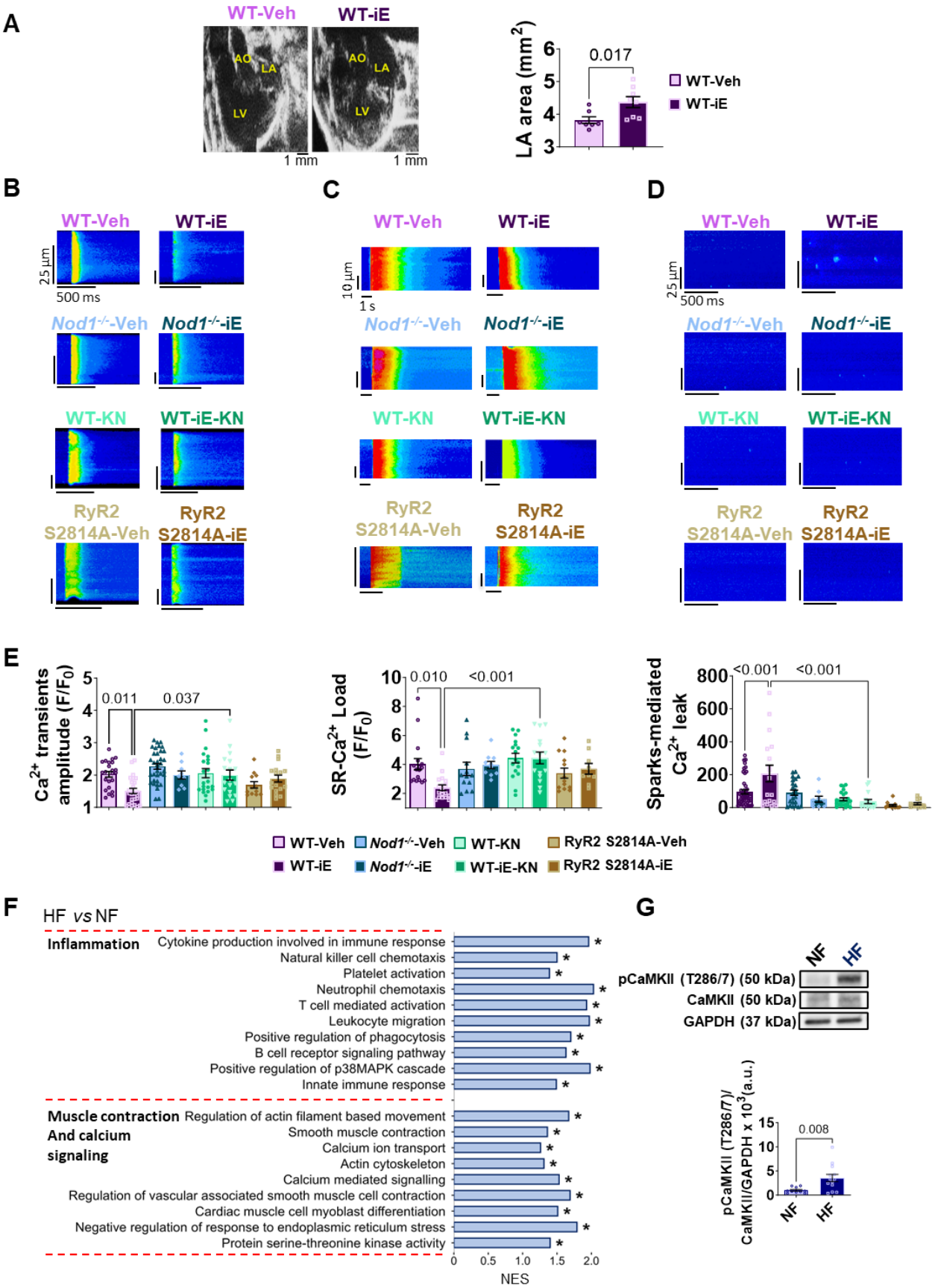
A
WT-Veh
WT-iE
AO
LA
LV
1 mm
1 mm
LA area (mm²)
0.017
WT-Veh
WT-iE
B
C
D
25 µm
500 ms
10 µm
1 s
Nod1-/--Veh
Nod1-/--iE
WT-KN
WT-iE-KN
RyR2 S2814A-Veh
RyR2 S2814A-iE
E
Ca2+ transients amplitude (F/F0)
0.011
0.037
SR-Ca2+ Load (F/F0)
0.010
<0.001
Sparks-mediated Ca2+ leak
<0.001
<0.001
F
HF vs NF
Inflammation
Cytokine production involved in immune response
Natural killer cell chemotaxis
Platelet activation
Neutrophil chemotaxis
T cell mediated activation
Leukocyte migration
Positive regulation of phagocytosis
B cell receptor signaling pathway
Positive regulation of p38MAPK cascade
Innate immune response
Muscle contraction And calcium signaling
Regulation of actin filament based movement
Smooth muscle contraction
Calcium ion transport
Actin cytoskeleton
Calcium mediated signalling
Regulation of vascular associated smooth muscle cell contraction
Cardiac muscle cell myoblast differentiation
Negative regulation of response to endoplasmic reticulum stress
Protein serine-threonine kinase activity
NES
G
NF
HF
pCaMKII (T286/7) (50 kDa)
CaMKII (50 kDa)
GAPDH (37 kDa)
pCaMKII (T286/7)/ CaMKII/GAPDH x 10³(a.u.)
0.008

796

Figure 4. NOD1 activation induces CaMKII-dependent Ca^{2+} mishandling in atrial cardiomyocytes. RNAseq analysis of human atrial myocardium. WT, *Nod1*$^{-/-}$, and *RyR2*-S2814A mice were used to assess the effects of genetic and pharmacological NOD1 modulation. (A) Representative echocardiographic images (left panel) and LA area (right panel) in WT-Vehicle (WT-Veh) and WT-C12-iE-DAP (WT-iE). (B-E) Representative confocal line-scan images and quantification of Ca^{2+} transients amplitude (C and E, left panel), SR Ca^{2+} load (C and E, central panel), and sparks-mediated diastolic Ca^{2+} leak (D and E, right panel) in WT-Veh (n = 17-47 cells/6 mice), WT-iE (n = 18-26 cells/3 mice), *Nod1*$^{-/-}$-Veh (n = 13-35 cells/3 mice), *Nod1*$^{-/-}$-iE (n = 9-10 cells/2 mice), WT-KN (n = 17-27 cells/4 mice), WT-iE-KN (n = 15-18 cells/3 mice), RyR2 S2814A-Veh (n = 12-13 cells/3 mice) and RyR2 S2814A-iE (n = 9-17 cells/3 mice). (F) Transcriptomic gene set enrichment analysis of human atrial tissue showing upregulation of inflammation- and Ca^{2+}-related pathways in HF vs. NF patients. * indicates significantly enriched pathways at FDR < 0.05. (G) Representative Western blot (upper panel) and quantification (lower panel) of CaMKII phosphorylation at Thr-286/7 (pCaMKII T286/7), normalized to total CaMKII and GAPDH (NF, n = 15; HF, n = 17). Data are mean ± SEM; statistical analyses performed by unpaired t-test or nested ANOVA (P < 0.05 considered significant).